GEOPHYSICS, VOL. 65, NO. 4 (JULY-AUGUST 2000); P. 1272–1280, 10 FIGS., 1 TABLE.

Predicting the seismic implications of salt anisotropy using numerical simulations of halite deformation

Daniel G. Raymer*, Andréa Tommasi‡, and J-Michael Kendall*

ABSTRACT

In the past, the potential for seismic anisotropy in salt structures and its effect on their seismic imaging has received little attention. We consider the plausibility of salt anisotropy through linked numerical studies of salt deformation and its seismic consequences. Numerical models are used to predict lattice preferred orientations (LPOs) in halite polycrystalline aggregates subjected to axial extension and simple shear. The elastic constants for the deformed polycrystalline aggregate are then calculated. Simple models representing a salt sill and the stem of a diapir are created using these elastic constants. Ray tracing is used to investigate the effects of halite LPO on the propagation of seismic waves. The results suggest that salt anisotropy can cause significant traveltime effects and could lead to significant errors in seismic interpretation in salt environments if this anisotropy is ignored. We also investigate potential amplitude variation with offset and azimuth (AVOA) for the reflection from the top and bottom of an anisotropic salt sill. Ray paths with a shear-wave leg within the salt display strong AVOA effects with a clear four-fold symmetry.

INTRODUCTION

The seismic imaging of salt structure environments can be difficult. This is due to the fact that salt flows easily, creating complex structures, and that there are large velocity contrasts between the high-velocity salt and the surrounding lower velocity sediments. The improvement of seismic images around salt structures is of interest to the exploration industry as subtle hydrocarbon traps are often associated with salt. An area of increasing concern is that of subsalt exploration, where the salt distorts the underlying image.

We investigate seismic anisotropy due to the lattice preferred orientation (LPO) of crystals which develops during salt deformation. Halite (NaCl) is the main constituent of many salt bodies. Although optically isotropic, halite crystals are elastically anisotropic with single crystal seismic anisotropies of 7.0% and 16.4% for the *P*- and *S*-waves, respectively. The effects of salt anisotropy on seismic images have received little prior attention. In a study of shear-wave splitting, Sun (1994) showed evidence for potash (approximately 75% NaCl, 25% KCl) anisotropy. Raymer and Kendall (1998) investigated the possible effects of salt anisotropy on seismic wave propagation but lacked constraints on the level of anisotropy likely to occur. In our current work, LPO due to halite deformation is predicted through numerical simulation. Laboratory and field measurements of deformation-induced LPO in halite (e.g., Schwerdtner, 1968; Skrotzki and Welch, 1983; Kern and Richter, 1985) provide constraints for our simulations.

The flow of salt and the resulting formation of a wide range of structures is a complicated process. In this work, we consider two types of deformation that are usual in salt bodies: simple shear and axial extension. Shear zones are known to occur at the edges of salt bodies and within sills (Talbot and Jackson, 1987). Axial extension is expected in the central region of diapir stems. The effective elastic constants of the deformed polycrystalline aggregate are then used to construct a range of seismic models based on salt flow in a horizontal salt sill and the stem of a diapir. The seismic implications of the salt anisotropy on traveltimes and amplitudes are investigated by ray tracing through the models.

SIMULATED DEFORMATION

It is well known that solid-state deformation of polycrystalline materials by dislocation creep gives rise to crystallographic fabrics and, if the constituent crystals are elastically anisotropic, to seismic anisotropy. Evidence of seismic anisotropy therefore provides information on the deformation

Presented at the 68th Annual International Meeting, Society of Exploration Geophysicists. Manuscript received by the Editor April 5, 1999; revised manuscript received December 17, 1999.
*University of Leeds, School of Earth Sciences, Woodhouse Lane, Leeds LS2 9JT, United Kingdom. E-mail: d.raymer@earth.leeds.ac.uk; m.kendall@earth.leeds.ac.uk.
‡Formerly University of Leeds, School of Earth Sciences, Leeds, United Kingdom; presently Laboratoire de Tectonophysique, Universite Montpellier II, Place Eugène Batillon, 34095 Montpellier Cedex 05, France. E-mail: deia@dstu.univ-montp2.fr.

of the studied domain. In this section, we present numerical simulations of halite deformation.

Under experimental and natural conditions, halite polycrystals deform dominantly by dislocation creep; in other words, they deform by a combination of dislocation glide on various crystallographic planes, dislocation climb, and dynamic recrystalization (e.g., Muehlberger and Clabaugh, 1968; Schwerdtner, 1968; Urai et al., 1987; Carter et al., 1993). In addition, the presence of even small amounts of water results in extensive dynamic recrystallization by grain-boundary migration at relatively low-temperature conditions (<100°C) that prevail during natural deformation (Urai et al., 1987). The presence of saturated brines may also result in activation of solution-precipitation processes (Spiers et al., 1990).

During dislocation creep, LPO development results essentially from dislocation glide, since climb does not produce crystal reorientation and recrystallization processes mainly modify LPO intensities. Whereas recrystalization by subgrain rotation induces a dispersion of the LPO, grain boundary migration (the dominant recrystallization process in halite polycrystals in presence of water) tends to strenghten the low-energy orientations (Urai et al., 1987). Thus halite LPO formed during rock salt deformation may be approached through polycrystal plasticity models.

These models simulate the deformation of a polycrystal based on two assumptions: (1) LPO development is controlled by intracrystalline slip on a few crystallographic systems (i.e., dislocation glide only), and (2) the polycrystal behavior may be calculated as an average of the grains' responses. Such polycrystal plasticity models have already been coupled to geodynamic simulations in order to study the development of olivine LPO and seismic anisotropy within the upper mantle (Chastel et al., 1993; Blackman et al., 1996; Tommasi, 1998).

In this paper, we use the anisotropic viscoplastic self-consistent model (VPSC) developed by Lebensohn and Tome (1993) to predict the LPO developed by halite polycrystals submitted to simple shear and axial extension. A complete description of the model may be found in Lebensohn and Tome (1993). In the next paragraphs, we briefly review its principles.

At the grain scale, the shear rate ($\dot{\gamma}^s$) in slip system s is related to the local deviatoric stress tensor **s** by,

$$\dot{\gamma}^s = \dot{\gamma}_0 \left(\frac{\tau_r^s}{\tau_0^s} \right)^{n^s} = \dot{\gamma}_0 \left(\frac{r_{ij}^s s_{ij}}{\tau_0^s} \right)^{n^s}, \qquad (1)$$

where $\dot{\gamma}_0$ is a reference rate, taken as 1 s^{-1}. The terms n^s, τ_r^s, and τ_o^s are, respectively, the stress exponent, the resolved shear stress, and the reference resolved shear stress for the system s, whose orientation relative to the macroscopic axes is expressed by $\mathbf{r}^s$. The sum of the shear rates over all slip systems gives the grain's shear rate $\dot{\varepsilon}_{ij}$.

For a given microscopic constitutive relation (i.e., a set of reference shear stresses and stress exponents for all active slip systems), an initial LPO, and an imposed deformation, the VPSC model calculates the stress and strain rate (s, $\dot{\varepsilon}$) in each grain based on the assumption that their volume averages equal the stress and strain ($\bar{\Sigma}$, $\dot{E}$) of the polycrystal. Interactions between a grain and its surroundings are approached by the interaction between an ellipsoidal inclusion with similar lattice orientation and an infinite homogeneous equivalent medium, whose behavior is the weighted average of the behavior of all grains. This leads to an interaction equation that relates local stresses and strain rates to the macroscopic quantities

$$\dot{\varepsilon}_{ij} - \dot{E}_{ij} = -\tilde{M}_{ijkl}(s_{kl} - \bar{\Sigma}_{kl}), \qquad (2)$$

where $\tilde{\mathbf{M}}$ is the interaction tensor that depends on the rheological properties of the aggregate and on the shape of the grains.

Numerical convergence is achieved when the relative difference between average and macroscopic quantities is less than 0.03. Grain shapes are then updated and the reorientation of each grain is calculated. The lattice rotation rate for each grain (relative to the macroscopic axes) is given by

$$\dot{\omega}_{ij} = \dot{\Omega}_{ij} - \omega_{ij}^P + \tilde{\omega}_{ij}, \qquad (3)$$

where $\dot{\Omega}$ is the macroscopic spin (i.e., the antisymmetric component of the imposed macroscopic velocity gradient **L**), ω^P is the plastic spin associated with the grain plastic deformation, and $\tilde{\omega}$ is the reorientation rate of the associated ellipsoidal inclusion, which depends on the difference in strain rate between the grain and the polycrystal, and increases with ellipsoid distortion (i.e., with increasing deformation).

Halite deforms through slip on {110}⟨110⟩, {100}⟨110⟩, and {111}⟨110⟩ systems. Under experimental conditions and room temperatures, the {110}⟨110⟩ slip system is the most easily activated, being 6–7 times weaker than the other systems, but differences in critical resolved shear stresses vanish at higher temperatures (Carter and Heard, 1970). Textures observed in naturally deformed rocksalt (Carter and Hansen, 1983; Kern and Richter, 1985) are better reproduced using low temperature data (Figure 1). In this study, as in previous LPO modeling by Wenk et al. (1989), critical resolved shear stresses are taken as 5 MPa for {110} slip and 33 MPa for both {100} and {111} slip, and the stress exponent n^s is 9.

LPO development for both axial extension and simple shear is calculated for polycrystalline aggregates composed of 200 grains. Before deformation, the grains are spherical and display random LPOs. The strain history is imposed through a macroscopic velocity gradient tensor **L** for simple shear (4) and axial extension (5):

$$\begin{pmatrix} 1 & 0 & 0 \\ 0 & -1/2 & 0 \\ 0 & 0 & -1/2 \end{pmatrix} \qquad (4)$$

$$\begin{pmatrix} 0 & 1 & 0 \\ 0 & 0 & 0 \\ 0 & 0 & 0 \end{pmatrix} \qquad (5)$$

The predicted orientations of the ⟨100⟩ halite crystallographic axes for both deformations are shown in Figure 2. Note the similarity between Figures 2a, b, d, and e and Figure 1a. Simple shear is characterized by concentration of ⟨100⟩ axes within and normal to the foliation (schistosity). As strain increases, ⟨100⟩ axes within the foliation form two weak maxima oblique to the shear direction. LPO development in axial extension is characterized by ⟨100⟩ axes oriented parallel and normal to the extension direction.

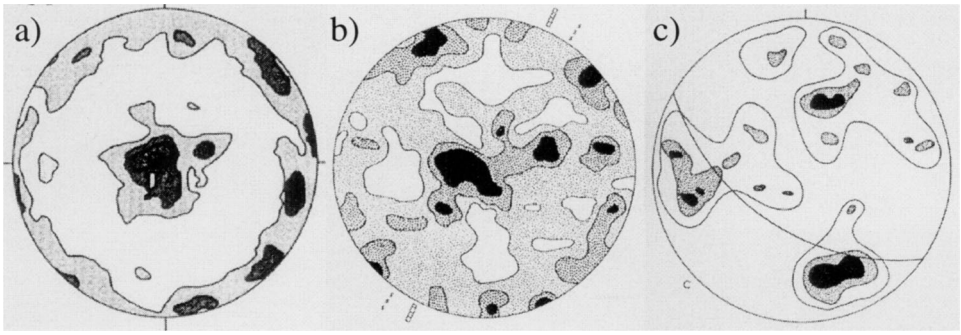

FIG. 1. Preferred orientations of the ⟨100⟩ halite crystallographic axes for naturally deformed rock salt plotted as a lower hemisphere stereographic equal area projection. Contours are given in unit multiples of a random distribution (m.r.d.). (a) Rock salt from Asse anticline (Germany); foliation is horizontal (Kern and Richter, 1985). (b) Specimen from Winnfield salt dome (Schwerdtner, 1968). (c) Specimen from Grand Saline dome. The great circle indicates axial plane of folds (Muehlberger and Clabaugh, 1968).

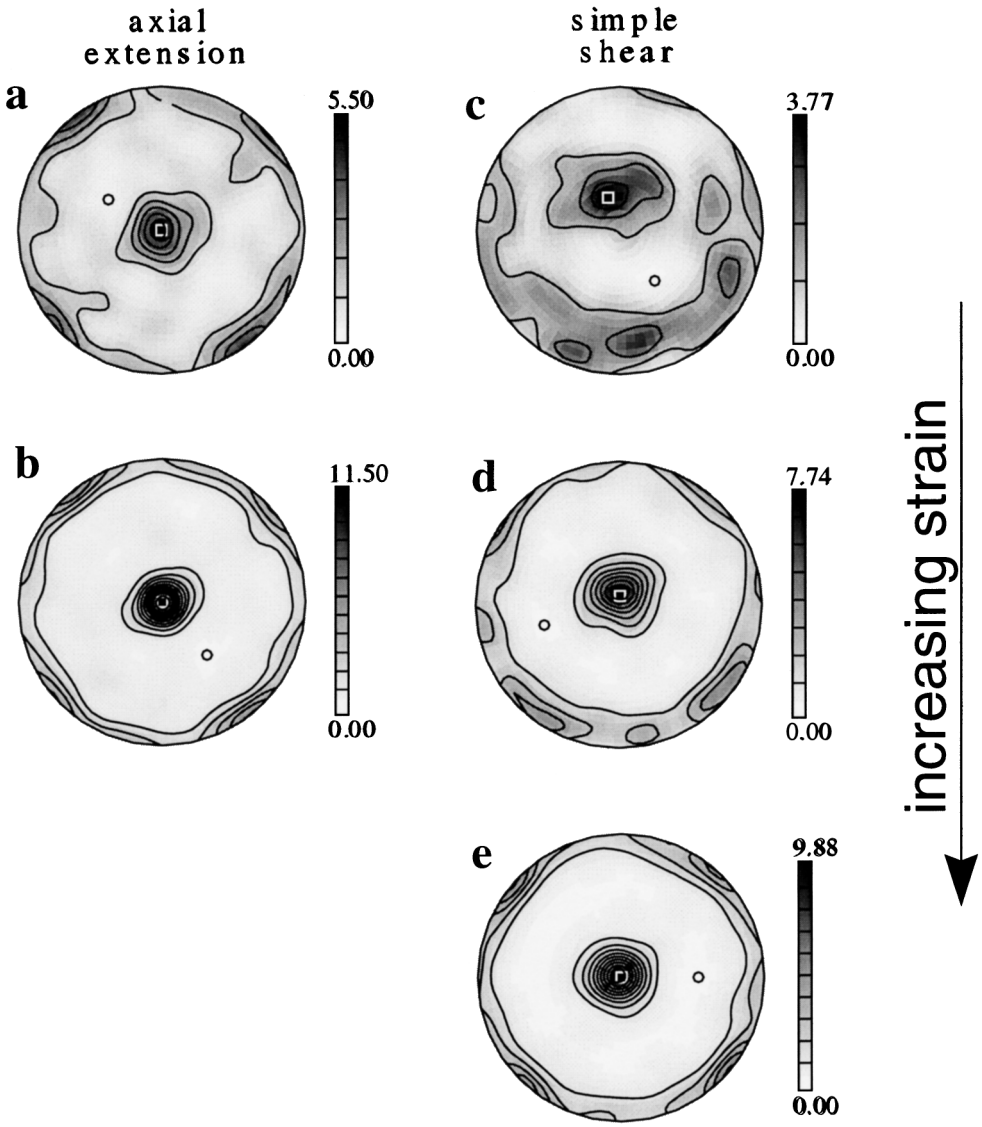

FIG. 2. Predicted orientations of the ⟨100⟩ halite crystallographic axes for a halite polycrystal submitted to (a) 100% and (b) 200% axial extension, and shear strains of (c) 1.5, (d) 5, and (e) 10. Extension direction is vertical. The shear plane is horizontal, shear direction north-south, and the shear in upper hemisphere is towards the south. Stereographic equal area projection, lower hemisphere, 200 grains. Contours are given in unit multiples of a random distribution (m.r.d.).

ELASTIC PROPERTIES

In each deformed aggregate, the LPO of each grain is described by three Euler angles: φ, θ, and ϕ. The information we require for seismic modeling is the effective elastic parameters of the deformed polycrystalline halite aggregate. The effective elastic parameters can be calculated using the individual grain orientations and the elastic properties of a single halite crystal. The halite single crystal stiffnesses used are $C_{11} = 49.1$, $C_{12} = 14.0$, and $C_{44} = 12.7$ (in gigapascals), and the halite density is taken as $\rho = 2160$ kg/m^3 (Gebrande, 1982). For each grain, the halite single crystal stiffness tensor **C** is rotated by the Euler angles giving the stiffness tensor $\mathbf{C}^n$ for that LPO. To obtain the effective elastic constants of the polycrystalline aggregate, the average of all the rotated elastic constants is calculated. The average was carried out using both the stiffness tensor **C** and the compliance tensor **S**. The average of the stiffnesses is known as a Voigt average and assumes uniformity of strain across grain boundaries:

$$C_{ij}^V = \frac{1}{200}\sum_{n=1}^{200} C_{ij}^n. \tag{6}$$

The Reuss average is calculated using the compliances and assumes uniformity of stress across the grain boundaries; the average compliances can then be inverted to give the stiffnesses:

$$S_{ij}^R = \frac{1}{200}\sum_{n=1}^{200} S_{ij}^n,$$

$$\mathbf{C}^R = (\mathbf{S}^R)^{-1}. \tag{7}$$

These two averages form an upper (Voigt) and lower (Reuss) limit to the value of the elastic parameters of the aggregate. The value we use in modeling is the Voigt-Reuss-Hill (VRH) average proposed by Hill (1952), which is the average of the two results above:

$$C_{ij}^{VRH} = \frac{C_{ij}^V + C_{ij}^R}{2}. \tag{8}$$

The stiffnessess obtained for the four halite aggregates used in the subsequent seismic modeling are shown in Table 1. For a given wave-front normal and a set of elastic constants, the group velocity can be calculated using standard methods (Kendall and Thomson, 1989). Calculation of velocities over a range of normals defines the anisotropic velocity surface.

Plots showing the projection of the velocities onto a unit sphere are created to view the 3-D velocity distribution for polycrystalline aggregates after axial extension with 200% strain (Figure 3a) and simple shear with 600% strain (shear strain 10) (Figure 3b). For simple shear, strain intensity is usually given in terms of the shear strain (i.e., displacement/width of the shear zone); we will use this measure from now on. The seismic velocities vary with propagation direction, so the aggregates are clearly anisotropic. The location of the maximum and minimum velocities are recorded, and these values are used to calculate the percent anisotropy for the *P*-, *S*1-, and *S*2-waves. Here the shear waves are sorted by their velocities with *S*1 the faster of the two shear waves. The shear wave splitting is also calculated for each direction. This is the difference between the *S*1 and *S*2 velocity in a given direction; the maximum and minimum splitting is also given as a percentage of the average *S*-wave velocity in that direction.

Both Figures 3a and 3b show a clear four-fold symmetry axis along the *x*-axis (the extension direction) for axial extension and the *y*-axis (the normal to the shear plane) for simple shear. The constants calculated for each polycrystalline aggregate are triclinic (21 independent elastic constants), but there is clearly higher symmetry present. To simplify the modeling, we approximated the elastic constants with a higher symmetry, as suggested by Kendall et al. (1998) in mantle flow modeling. As the strain increases, the elasticity can be approximated by higher symmetries (e.g., orthorhombic) with the limiting case being hexagonal symmetry. Nevertheless, we use monoclinic symmetry in our seismic modeling as it is a good approximation for all of our models. The eight elastic constants that are set to zero to approximate monoclinic symmetry are italicized in Table 1.

Figure 4 shows the change in *P*-wave anisotropy and the maximum shear-wave splitting with increasing strain for three different types of deformation: low-temperature axial extension, low-temperature simple shear, and high-temperature simple shear. In each case, an increase in strain results in an increase in anisotropy, but the rate of change reduces with increasing strain.

RAY TRACING AND RESULTS

Traveltime effects

Two models are created which provide an idealized 2-D representation of a horizontal salt sill (Figure 5) and the stem of a diapir (Figure 6). In the horizontal salt sill, we consider deformation consisting entirely of simple shear in the *x*-direction. A strain gradient from the edges to the center of the sill is

Table 1. Elastic stiffness calculated from numerical simulation of halite deformation for axial extension at 200% strain and simple shear with shear strains of 1.5, 5, and 10.*

Stiffness (GPa)	200% Axial extension	Shear strain		
		1.5	5.0	10
C_{11}	47.3	45.1	45.8	45.7
C_{12}	14.9	16.1	14.8	14.5
C_{13}	14.9	15.9	16.5	16.9
C_{14}	*0.0*	*0.0*	*0.0*	*0.0*
C_{15}	−0.1	*−0.1*	*−0.1*	*−0.1*
C_{16}	*0.1*	0.9	0.6	0.1
C_{22}	45.6	45.1	47.4	48.0
C_{23}	16.6	15.9	14.8	14.6
C_{24}	*0.1*	*0.0*	*0.1*	*0.0*
C_{25}	0.0	*0.0*	*0.0*	*0.0*
C_{26}	*0.0*	−1.0	−0.8	−0.2
C_{33}	45.7	45.3	45.8	45.6
C_{34}	*0.0*	*0.0*	*0.0*	*0.0*
C_{35}	0.1	*0.1*	*0.1*	*0.0*
C_{36}	*0.0*	0.1	0.3	0.0
C_{44}	15.0	14.3	13.4	13.1
C_{45}	*0.0*	0.1	0.2	0.0
C_{46}	0.0	*0.0*	*0.0*	*0.0*
C_{55}	13.4	14.3	14.9	15.3
C_{56}	*0.0*	*0.0*	*0.0*	*0.0*
C_{66}	13.4	14.6	13.4	13.1

*The elastic stiffnesses are expressed in Voigt notation with values in italics indicating those that are set to zero to approximate monoclinic symmetry. The elastic constants have a monoclinic symmetry, but the high strain cases can be approximated by a hexagonal symmetry.

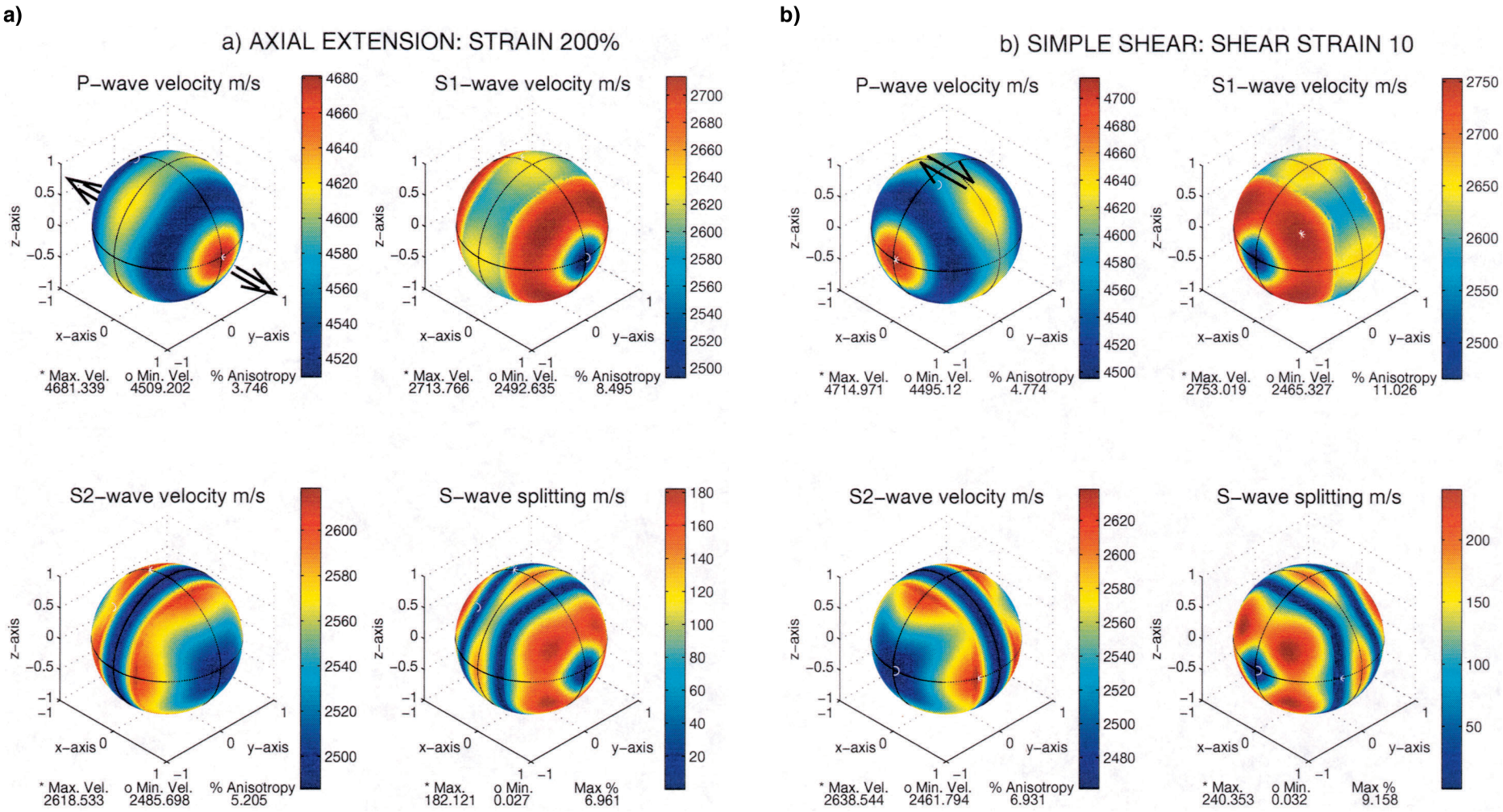

FIG. 3. Projections of seismic velocities and shear wave splitting onto a unit sphere for two of the polycrystalline aggregates used in modeling. (a) Axial extension at 200% strain; extension is along the x-axis as indicated by arrows on the first sphere. (b) Simple shear at shear strain of 10; the plane of shear is the x-z-plane with right lateral (dextral) motion in the x direction. Arrows indicate the sense of shear in the first sphere. Values of maximum and minimum velocities and the percent anisotropy are given below each plot.

simulated using six layers with different elastic constants, which range from those for a shear strain of 10 (600% strain) near the sill walls to 1.5 (100% strain) at the center of the sill (Figure 5).

In the vertical diapir stem, we consider a deformation characterized by simple shear near the stem walls and axial extension in the central region. The sense of shear and axial extension are in the z-direction. The layers of simple shear have a shear strain of 10 (600% strain) and the homogeneous central region has axial extension with 200% strain (Figure 6). The selection of strain is somewhat arbitrary, but regions of high shear strain are known to exist at the edges of diapir stems and other structures where salt has flowed (Talbot and Jackson, 1987). In both models, only the salt is anisotropic; the rest of the model is taken to be an isotropic shale with velocities $V_P = 2800$ m/s and $V_S = 1600$ m/s, and density $\rho = 2400$ kg/m^3.

The software package ATRAK, which traces seismic rays in 3-D, multilayered, inhomogeneous, anisotropic media, was used to model wave propagation through the models. The program is based on asymptotic ray theory (Guest and Kendall, 1993). *P*-, *S*1-, and *S*2-waves are considered, and the shear waves are sorted by polarization with the *S*1-wave being the most vertically polarized.

Rays are traced through the salt sill (Figure 5) from a point source at the top of the model in the isotropic shale and reflected off the base of the salt at the interface with the shale below. The surface seismic line is parallel to the direction of shear. For the diapir stem (Figure 6), rays are traced to simulate a vertical seismic profile configuration. Rays are traced from the isotropic shale through the salt to a vertical borehole in the shale. For comparison, ray tracing is also done for an isotropic version of each model where the salt had no LPO, seismic velocities $V_P = 4560$ m/s and $V_S = 2580$ m/s, and density $\rho = 2160$ kg/m^3.

The deviation of ray paths in Figure 5 clearly shows the effect of the variation in LPO within the salt sill. Traveltimes for rays traced in the anisotropic and isotropic models show differences of up to 5 ms for *P*-wave, 20 ms for *S*1-wave, and 15 ms for *S*2-waves. All show a change in the sign of the time differences with an increase in offset, and shear-wave splitting of up to 25 ms can occur. Ray tracing through the diapir stem (Figure 6) also shows significant traveltime differences caused by the salt anisotropy. Differences of up to 10, 50, and 35 ms are seen for the *P*-, *S*1-, and *S*2-waves, respectively, with the *S*1-wave values showing considerable variation with depth. Shear-wave splitting of up to 60 ms is visible. Although these models are idealized, they demonstrate the potentially large traveltime effects that may occur in reality.

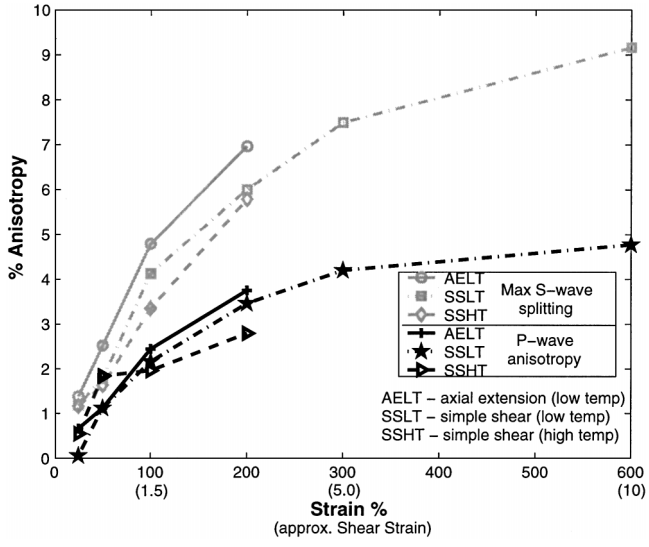

FIG. 4. Graph showing the change in *P*-wave anisotropy and the maximum shear-wave splitting with increasing strain for three different deformation regimes: axial extension (low temperature), simple shear (low temperature) and simple shear (high temperature).

AVOA and converted waves

To investigate the amplitude variation with offset and azimuth (AVOA), a 3-D version of a horizontal salt sill is created (Figure 7). This model has layers of simple shear salt, where both layers have shear strain of 10 (600% strain), but with an opposite sense of shear. The shot location is at zero ($x = 0$, $y = 0$) offset and *P*, *S*1 and *S*2 reflections from the top and the base of the salt including conversions are considered. Three combinations of *P* to *S* conversions for both *S*1- and *S*2-waves are modeled; these are *PSSS*, *PPSS*, and *PSSP*. The four letters refer to the different ray legs in the model: above salt (1 and 4), within salt (2 and 3), downgoing (1 and 2) and upcoming (3 and 4). Thus, *P*-*S*1-*S*1-*P* is a *P*-wave converting to

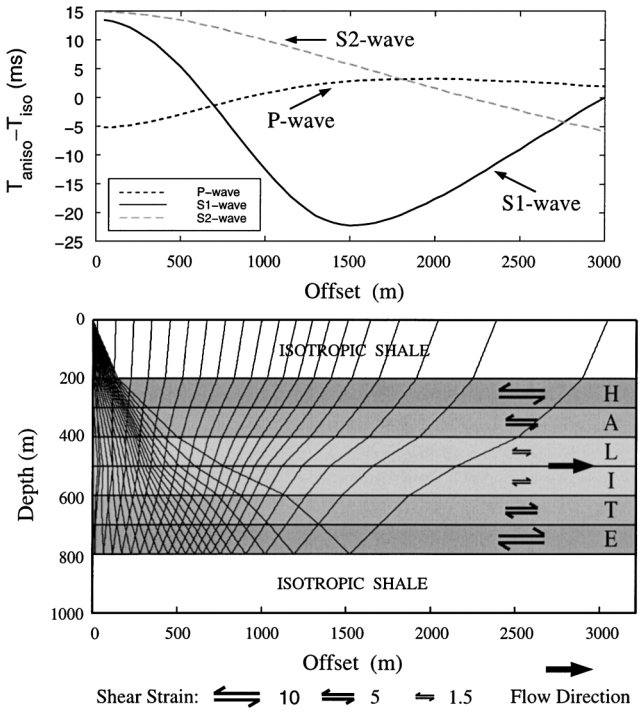

FIG. 5. Model of flow in a horizontal salt (halite) sill. The deformation consists entirely of simple shear with shear strain decreasing from 10 at the edges to 1.5 in the center. Rays traced through the resulting elastic model are shown for the *S*1-wave traced from a common shotpoint and reflecting off the base of the salt sill. The graph above shows the difference between the *P*-, *S*1-, and *S*2-wave traveltimes for the anisotropic and isotropic models.

*S*1 at the top of salt, remaining a *S*1-wave after reflection at the base of salt then converting back to *P*-wave on exiting the salt.

The amplitudes of rays reflected from the top of the salt layer (Figure 8) show only small variations with azimuth. The effects seen here arise solely from the reflection/transmission (R/T) coefficients as the ray paths are entirely in an isotropic medium and the geometrical spreading is equal for all azimuths.

For reflections from the base of the salt (Figure 9), the variations in amplitudes depend on the variation in R/T coefficients and also azimuthal variations in the ray path due to propagation through the anisotropic salt. The *P*-wave reflection off the base of the salt shows no observable variation in amplitude with azimuth, but the two shear waves show considerable variation. The *S*1 plot shows azimuthal variation at the center and, at far offsets amplitude, highs are visible on the diagonal to the *x*- and *y*-axes. This four-fold symmetry can also be seen in the velocity plot in Figure 3b. The *S*2 plot has generally higher amplitudes along the *x*- and *y*-axes but at very short offsets there are higher amplitudes in the *x* axis, which is the line of flow.

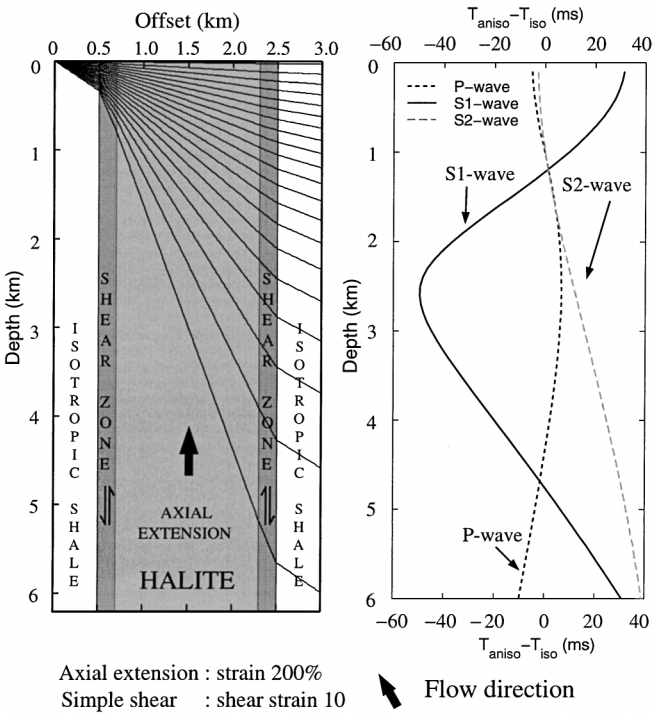

FIG. 6. On the left is a model of vertical flow in the stem of a diapir which also shows the ray paths for the *P*-waves. The halite deformation consists of a 200-m zone of simple shear with shear strain of 10 (600% strain) at the stem edges and a central region of axial extension with 200% strain. The graph on the right shows the difference between the *P*-, *S*1-, and *S*2-wave traveltimes for anisotropic and isotropic models.

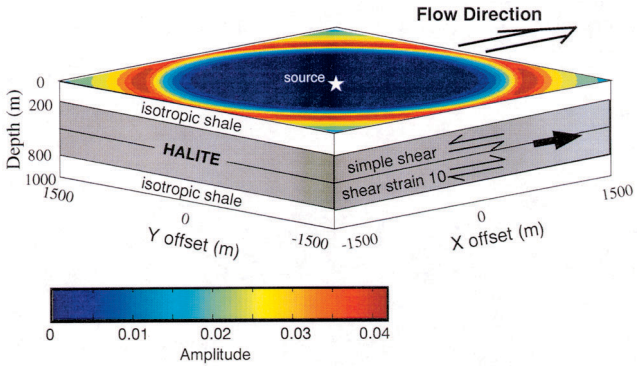

FIG. 7. Diagram of the 3-D salt sill model used to investigate AVOA effects due to anisotropic halite. The white star indicates the shot location ($x = 0, y = 0$). The surface of the model shows the ray amplitudes for *P*-waves converting to *S*1-waves at the top of the salt layer and reflecting at the base (*P*-*S*1-*S*1-*S*1).

The AVOA plots (Figure 10) for conversions from an initial *P*-wave show varying magnitudes of amplitude. The conversion to *S*1-wave on entering the salt (*P*-*S*1-*S*1-*S*1) has, at far offsets, amplitudes greater than any other wave type reflected at base of salt. Azimuthal variation can be seen with the amplitude highs occurring on the diagonals to the *x*- and *y*-axes. *P*-*S*1-*S*1-*P* has a similar pattern, but the second conversion causes reduced amplitudes. Some azimuthal variation can also be seen in the base salt conversion (*P*-*P*-*S*1-*S*1) with higher amplitudes and azimuthal variation at short offsets. For this model, the conversions from *P* to *S*2 are extremely weak due to the nearly transversely-isotropic (hexagonal) symmetry of the elastic parameters and the use of a flat layer model.

CONCLUSIONS AND DISCUSSIONS

Our numerical simulations of halite deformation by dislocation creep demonstrate that significant degrees of crystal orientation, LPO, can be reached, even with relatively low strains. As a consequence, the effective elastic constants for the modeled polycrystalline aggregates show that high levels of seismic anisotropy (5% *P*-wave anisotropy and 10% shear-wave splitting) are plausible. Ray tracing through models constructed using these elastic constants reveals large traveltime differences between the anisotropic and isotropic salt models. The greatest differences are seen for the shear waves, but the *P*-wave effects are still significant. Converted phases will also be strongly effected. The modeling shows that there should be large amounts of *S*-wave splitting within the salt in certain propagation directions, but it should be noted that there are directions where there will be no splitting.

Models of highly sheared salt show that there can be strong AVOA effects due to the salt anisotropy and that the azimuthal variations (AVA) show a clear four-fold symmetry. However, these effects are not visible with every phase. *P*-wave reflections from either the base or top of salt show little AVA. *S*-wave reflections from the top salt show little AVA, but base salt reflections show the four-fold symmetry. The amplitudes of the converted phases can be very large; in fact, at far offsets, the phase which converts to *S*1 on entering salt and reflects from its base (*P*-*S*1-*S*1-*S*1) has the largest amplitudes of any other base salt reflection. Phases which convert from *P* to *S*1 at the base salt show effects which are more pronounced at mid-range offsets than far offsets.

Although wave propagation effects due to salt anisotropy can be quite complicated, they hold a lot of valuable information about salt tectonics. Observations of the predicted seismic effects in seismic data will help prove the existence of large-scale salt anisotropy and offer insight into the type of deformation that has taken place. The existence of such anisotropy will mean that anisotropic methods will be required to obtain

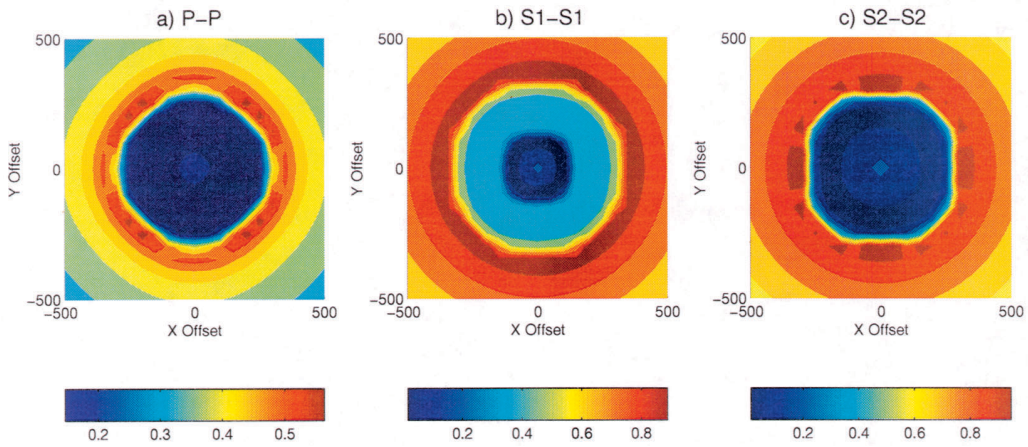

FIG. 8. AVOA plots for (a) *P*-, (b) *S*1-, and (c) *S*2-waves reflecting off the top of the 3-D horizontal salt sill (*PP* and *SS*). The source is located at the surface at offset (0, 0).

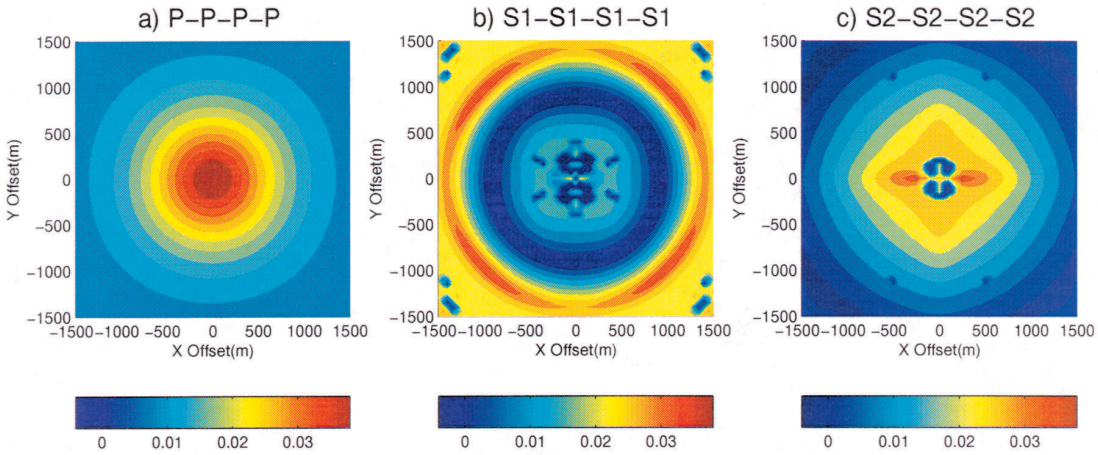

FIG. 9. AVOA plots for (a) *P*-, (b) *S*1-, and (c) *S*2-waves reflecting off the base of the horizontal salt sill (*PPPP* and *SSSS*). Source location at surface at offset (0, 0).

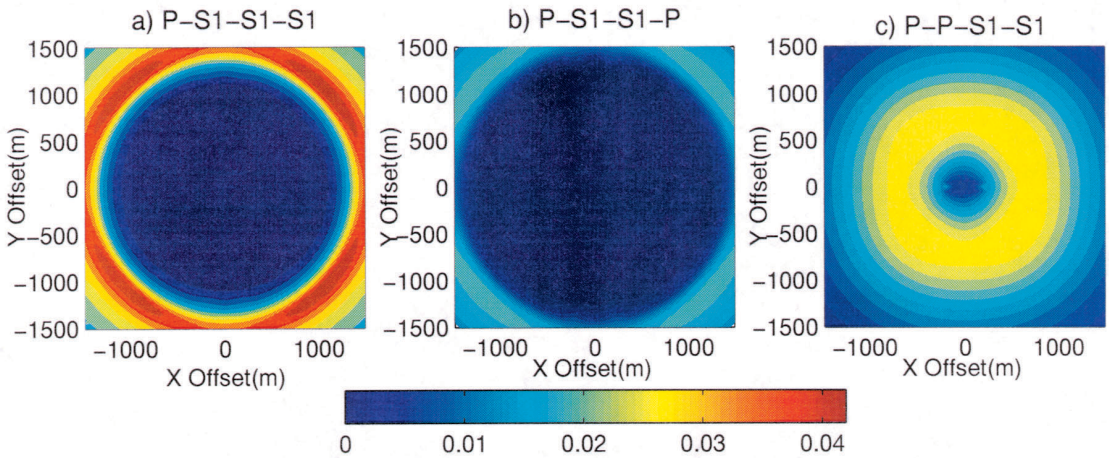

FIG. 10. AVOA plots for reflections off the base of the salt sill for waves that have undergone conversion from an initial *P*-wave to a *S*1-wave. (a) *P*-waves that have converted to an *S*-wave on entering the salt (*P*-*S*1-*S*1-*S*1). (b) Conversion from *P*-wave to *S*-wave on entering the salt then back to *P*-wave on exiting the salt (*P*-*S*1-*S*1-*P*). (c) Conversion from *P*-wave to *S*-wave on reflection at the base of the salt (*P*-*P*-*S*1-*S*1).

accurate imaging of salt and subsalt structures. For example, the location of subsalt targets may be mislocated due to the traveltime effects caused by the anisotropy.

This study raises a number of interesting issues for future investigation. The next obvious step is to look for effects of salt anisotropy in real data. Although three component recordings will be required to investigate shear and converted phases and shear-wave splitting, there is some potential to see these effects in conventional vertical-component data. Our flow modeling has been quite simple, so it would be instructive to consider the effects in more realistic flow structures, for example, the classic mushroom-shaped diapir. This will produce more complicated velocity structures, and there will be the issue of resolving the effects of heterogeneity from those due to the anisotropy. We also have not explored the competing effects from anisotropy in the surrounding media. Nevertheless, our study shows that salt anisotropy may be a significant factor to account for in the seismic exploration for oil and gas in salt environments.

ACKNOWLEDGMENTS

We thank Shell International Exploration and Production B.V. for the funding of this work. We thank the reviewers Edward Krebes, Jennifer Leslie, and Colin Sayers for their helpful comments regarding this paper. D. Raymer receives Ph.D. funding from NERC-UK.

REFERENCES

Blackman, D. K., Kendall, J.-M., Dawson, P., Wenk, H.-R., Boyce, D., and Phipps Morgan, J., 1996, Teleseismic imaging of subaxial flow at mid-ocean ridges: Travel-time effects of anisotropic mineral texture in the mantle: Geophys. J. Internat., **127**, 415–426.

Carter, N. L., and Hansen, F. D., 1983, Creep of rocksalt: Tectonophysics, **92**, 275–333.

Carter, N. L., and Heard, H. L., 1970, Temperature and rate-dependent deformation of halite: Am. J. Sci. **269**, 193–249.

Carter, N. L., Horseman, S. T., Russel, J. E., and Handin, J., 1993. Rheology of rocksalt: J. Struc. Geology, **15**, 1257–1271.

Chastel, T. B., Dawson, P. R., Wenk, H. R., and Bennett, K., 1993, Anisotropic convection with implications for the upper mantle: J. Geophys. Res. **98**, 17 757–17 771.

Gebrande, H., 1982, Elastic wave velocities and constants of elasticity of rocks and rock forming minerals, *in* Angenheister, G., Ed., Physical properties of rocks: Landolt-Börnstein, N.S. **V/1b**, 1–99.

Guest, W. S., and Kendall, J.-M., 1993, Modelling seismic waveforms in anisotropic inhomogeneous media using ray and Maslov asymptotic theory: Applications to exploration seismology: Can. J. Expl. Geophys. **29**, 78–92.

Hill, R., 1952, The elastic behaviour of a crystalline aggregate: Proc. Phys. Soc. (London), **A65**, 349–354.

Kendall, J.-M., Raymer, D. G., and Blackman, D. K., 1998, Bias due to simple approximations for flow-induced mineral orientation distribution: EOS, **79**, S212.

Kendall, J.-M., and Thomson, C. J., 1989, A comment on the form of the geometrical spreading equations, with some numerical examples of seismic ray tracing in inhomogeneous, anisotropic media: Geophys. J. Internat. **99**, 401–413.

Kern, R., and Richter, A., 1985, Microstructures and textures in evaporites, *in* Wenk, H.-R., Ed., Preferred orientation in deformed metals and rocks: An introduction to modern texture analysis: Academic Press, 317–333.

Lebensohn, R. A., and Tomé, C. N., 1993, A self-consistent anisotropic approach for the simulation of plastic deformation and texture development of polycrystals: Application to zirconium alloys: Acta Metall. **41**, 2611–2624.

Muehlberger, W. R., and Clabaugh, P. S., 1968, Internal structure and petrofabrics of Gulf Coast salt domes, *in* Braunstein, J., and O'Brien, G. D., Eds., Diapirism and diapirs: Am. Assn. Petr. Geol. Memoir **8**, 90–98.

Raymer, D. G., and Kendall, J.-M., 1998, Seismic anisotropy in salt structures due to preferred crystal orientation: Revue de l'Institut Français du Pétrole, **53**, 585–594.

Schwerdtner, W. M., 1968, Intergranular gliding in domal salt: Tectonophysics, **5**, 353–380.

Skrotzki, W., and Welch, P., 1983, Development of texture and micro structure in extruded ionic polycrystalline aggregates: Tectonophysics, **99**, 47–61.

Spiers, C. J., Schutjens, P. M. T. M., Brzesowsky, R. H., Peach, C. J., Liezenberg, J. L., and Zwart, H. J., 1990, Experimental determination of constitutive parameters governing creep of rocksalt by pressure solution, *in* Knipe, R. J., and Rutter, E. H., Eds., Deformation mechanisms, rheology, and tectonics: Geol. Soc. Spec. Pub. **54**, 215–227.

Sun, Z., 1994, Seismic anisotropy in salt from theoretical study, modelling, and field experiments: M.Sc. thesis, Univ. of Calgary.

Talbot, C. J., and Jackson, M. P. A., 1987, Internal kinematics of salt diapirs: AAPG Bull. **71**, 1068–1093.

Tommasi, A., 1998, Forward modelling of the development of seismic anisotropy in the upper mantle: Earth Planet. Sci. Lett., **160**, 1–13.

Urai, J. L., Spiers, C. J., Peach, C. J., Franssen, R. C. M. W., and Liezenberg, J. L., 1987, Deformation mechanisms in naturally deformed halite rocks as deduced from microstructural investigations: Geologie en Mijnbouw, **66**, 165–176.

Wenk, H.-R., Canova, G. R., Molinari, A., and Mecking, H., 1989, Texture development in halite: Comparison of Taylor model and self-consistent theory: Acta Metall., **37**, 2017–2029